ADVANCED SENSOR RESEARCH Open Access
www.advsensorres.com

Enhanced Broadband Photodetection with Geometry and Interface Engineered Nanocrystalline Graphite

*Devang Parmar, Simone Dehm, Naga Anirudh Peyyety, Sandeep Kumar, and Ralph Krupke**

Photodetection across the near-infrared (NIR) to short-wavelength infrared (SWIR) spectrum is important for many applications. This study explores photodetection using nanocrystalline graphite (NCG) in a suspended, narrow constriction configuration for improved performance. Bowtie constrictions are fabricated in both suspended and substrate-supported NCG devices, allowing for accurate comparison. It shows that the suspended constriction enhances the bolometric photoresponse and sensor detectivity by several orders of magnitude compared to the substrate-supported counterparts, attributed to reduced thermalization and electric field concentration. The suspended configuration preserves a spectrally flat photoresponse while reducing operating voltage through a tailored NCG layer thickness. Chromatic aberration-corrected photocurrent spectroscopy is used to measure the photoresponse from 1100 to 1700 nm, and diffraction-limited hyperspectral photocurrent imaging is conducted to measure the local photocurrent generation across the device. Bolometric and photo-thermoelectric currents are restricted to the suspended central constriction due to electric field concentration and thermal decoupling and the direction of the photocurrents within the sensor is revealed. The experimental data is complemented by simulations of the light absorption and the electric field distribution. This work indicates the importance of geometry and thermal decoupling for boosting device performance, offering promising prospects for sensitive and low-power NCG-based photodetectors in the NIR-SWIR range.

1. Introduction

Photodetection spanning the near-infrared (NIR) to short-wavelength infrared (SWIR) spectrum holds crucial significance across diverse domains, including telecommunications,[1] biomedical imaging,[2] food inspection,[3] night vision,[4] environmental monitoring,[5] and astronomy.[6] The materials employed for photodetection encompass bulk semiconductors such as InGaAs and Si,[7] as well as two-dimensional (2D) materials,[8,9] with the material's bandgap dictating the discernible wavelength range. Recently, newly emerging topological Dirac semimetal materials are being explored for their potential in wide wavelength range photodetection.[10–12] While graphene, as a zero-bandgap material, holds potential for broad-spectrum photodetection, its inherent light absorptance is intrinsically confined to a mere few percent.[13] Various strategies have been devised to enhance graphene's light absorption, involving its integration into plasmonic or photonic structures,[14,15] interfacing with quantum dots,[16] or other 2D materials.[17] Yet, these methods yield improved photoresponse only within limited wavelength ranges. Sustaining broadband absorption necessitates an increase in the number of layers, and through transfer matrix calculations, an optimal threshold of around 90 layers has been identified for achieving a flat spectral response.[18] However, synthesizing multilayer graphene/graphite films remains an unattainable endeavor. In contrast, nanocrystalline graphene or graphite (NCG) can be fabricated with precise thickness control by manipulating spin casting conditions and photoresist solution concentrations, prior to the graphitization process.[19,20] Our earlier work showcased photodetection utilizing NCG, exhibiting a spectrally flat photoresponse across the NIR to SWIR range.[21] The current study builds upon this foundation, focusing on elevating the photoresponse via the creation of a suspended, narrow NCG constriction as the sensing region.[22] By leveraging electric field concentration and thermal isolation, we achieve a bolometric photoresponse improvement by two orders of magnitude compared to substrate-supported NCG devices lacking such constriction. In doing so, we preserve the spectrally flat photoresponse from the

D. Parmar, S. Dehm, N. A. Peyyety, S. Kumar, R. Krupke
Institute of Nanotechnology
Karlsruhe Institute of Technology
76131 Karlsruhe, Germany
E-mail: ralph.krupke@kit.edu
D. Parmar, R. Krupke
Department of Materials Science
Technical University of Darmstadt
64287 Darmstadt, Germany
D. Parmar, R. Krupke
Institute of Quantum Materials and Technologies
Karlsruhe Institute of Technology
76131 Karlsruhe, Germany

The ORCID identification number(s) for the author(s) of this article can be found under https://doi.org/10.1002/adsr.202300134

DOI: 10.1002/adsr.202300134

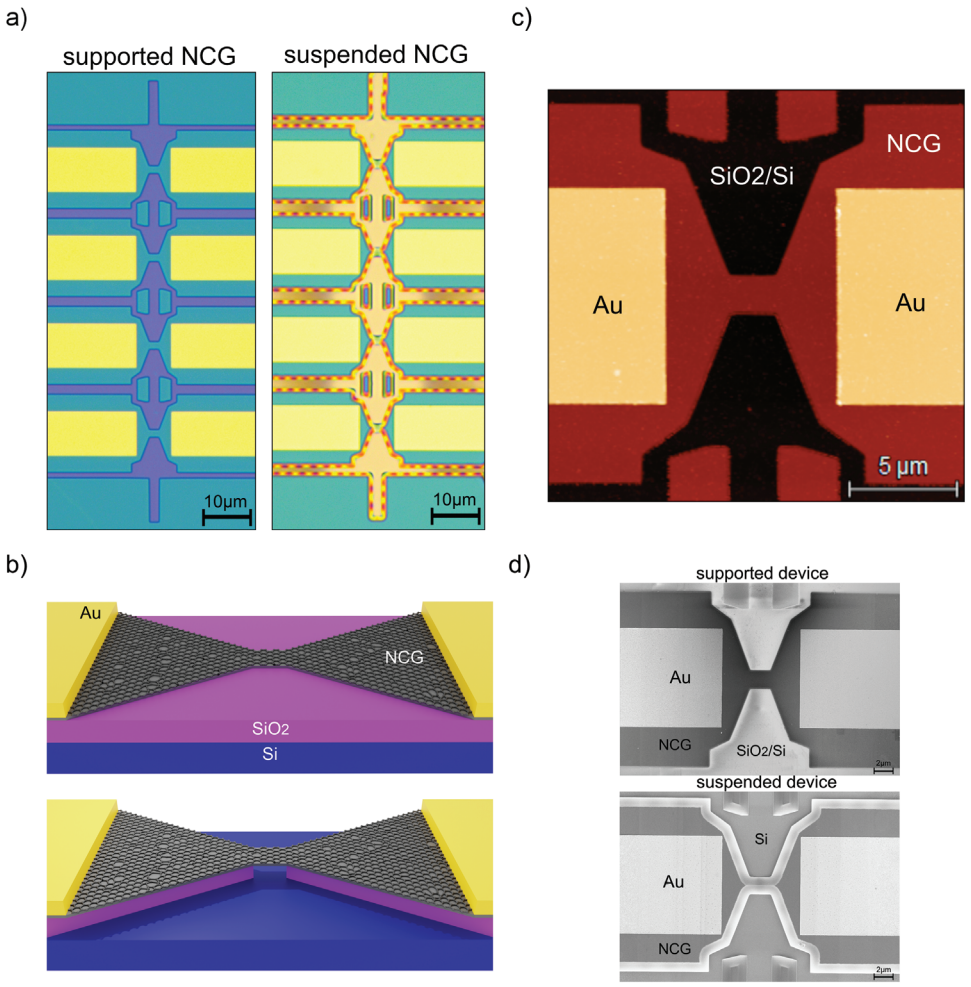

Figure 1. Microscopic characterization of nanocrystalline graphite (NCG) devices. a) True-color optical micrographs of NCG device arrays with substrate-supported and free-suspended bowtie constrictions (NCG: cyan, Au-electrodes: yellow, SiO_2: dark-blue, Si: light-brown). b) False-color atomic force microscope height image of a substrate-supported device (NCG thickness 36 nm). c) Schematic of devices with supported (top) and suspended (bottom) constrictions. d) Scanning electron micrographs of devices with supported and suspended constrictions. The suspended NCG segments appear brighter compared to the substrate-supported NCG regions. In all devices, the center of the bowtie constriction is 2μm × 2μm.

NIR to SWIR range, while concurrently reducing the operating voltage via increased NCG layer thickness.

2. Results and Discussion

Photodetectors were fabricated in two distinct configurations, as suspended and supported nanocrystalline graphite (NCG) devices with bowtie-like narrow constrictions. A total of four sets of suspended and an equivalent number of supported NCG photodetectors were fabricated on the same Si/SiO_2 substrate to facilitate accurate comparison, as shown in the optical microscopy images **Figure** 1a and the perspective drawing Figure 1b. Details on the fabrication process can be found in the Experimental Section. Briefly, NCG was synthesized by graphitization of a spin-casted photoresist layer on a 300nm-SiO_2/Si substrate. The optimum thickness for maximum absorption over a broad wavelength range was determined by transfer-matrix simulations.[21] Via multi-layer e-beam lithography, dry-etching, and metallization, the NCG was shaped into the desired form and contacted with 10 μm wide Au/Cr electrodes that were 8 μm apart. Between the electrodes, the NCG was tapered from 18 μm width down to a central constriction of 2 μm × 2 μm area, forming a bowtie-like structure, which can be seen in the atomic force microscopy (AFM) image Figure 1c. For the suspended configuration, the central area was under-etched by wet etching in buffered HF. Since NCG is inert against HF etching, the NCG pattern defines the area through which wet etching takes place. This enabled a complete etching of the SiO_2 underneath the constriction down to the Si, while the tapered regions remained supported by the SiO_2, as can be seen in the SEM image in Figure 1d. The thickness of the NCG film was measured by AFM, and the degree of sp^2 hybridization and the average crystallite size in the NCG films were determined by analysis of Raman data in **Figure** 2d. The Raman spectra show the characteristic broad D-, G-, and 2D-peaks for NCG at 1361, 1597, and 2700 cm^{-1}, respectively.[19,21] Similar to the previous study, where we investigated in detail the graphitization conditions using Raman spectroscopy and X-ray photoelectron spectroscopy (XPS),[19]

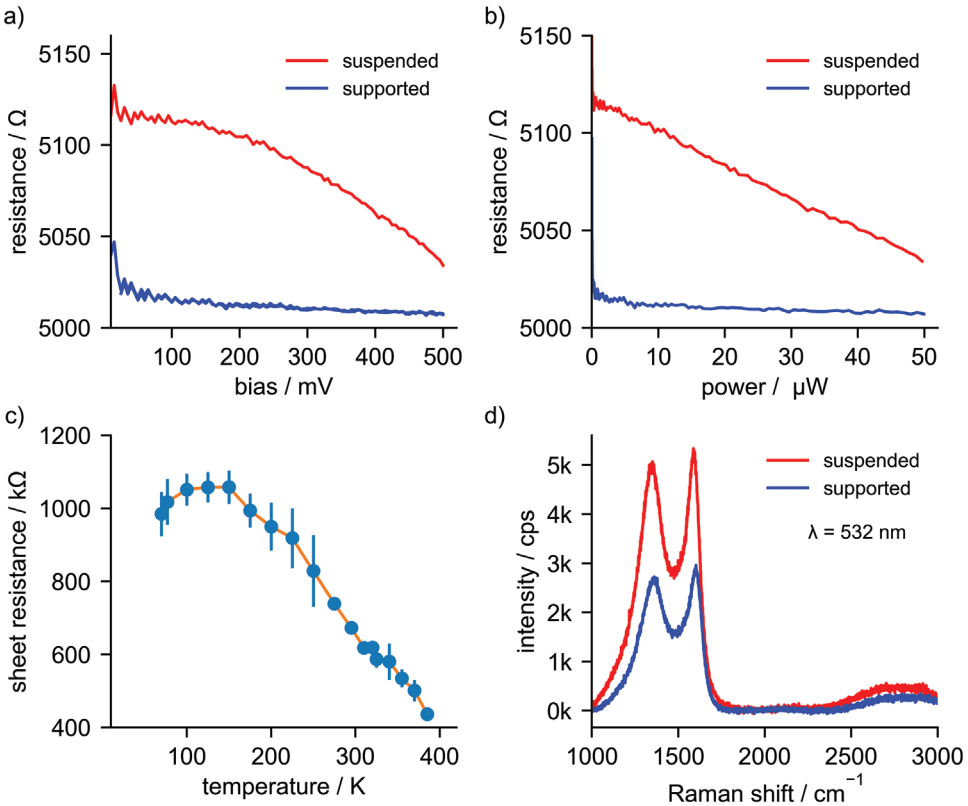

Figure 2. Electrical and Raman characterization of NCG devices. a) Device resistance versus bias voltage, and b) resistance vs electrical power dissipation ($P=V^2/R$), for supported and suspended constrictions. c) NCG sheet resistance versus temperature, data replicated from ref. [21] d) Raman spectra of NCG/300nm-SiO_2/Si (supported NCG) and NCG/300nm-air/Si (suspended NCG).

we employed a fitting technique that involved determining the position of the G-peak and the ratio of the D-mode and G-mode intensities to the hybridization trajectory proposed by Robertson and Ferrari.[23] This analysis confirmed that the NCG film was completely graphitized with nearly 100% sp^2 hybridization, as expected due to similar synthesis conditions.[19] The average crystallite size in the NCG film was determined by the full width at half maximum (FWHM) of the D-peak and found to be approximately 2–5 nm, consistent with our previous analyses using Raman spectroscopy and electron diffraction.[19,24–26] When comparing suspended and supported devices, the Raman signal intensity was markedly higher for the suspended NCG configuration compared to the supported counterpart, because of the preferential radiation of the Raman scattered light into the optically dense SiO_2/Si substrate medium.[27,28]

The electrical resistance of devices with substrate-supported and suspended constrictions was determined in a two-probe configuration in a probe station. From reference structures, we know that the resistance of the large-area contact between NCG and the metal, and the resistance of the metal leads is low and negligible compared to the resistance of the NCG bowtie structure. We have performed finite-element simulations on the planar device geometry and found that 39% of the two-probe resistance accounts for the central square-shaped constriction, which is close to 47% derived by analytic expression.[29] The remaining resistance is due to the tapered NCG regions. Figure 2a shows the resistance of the device R versus the applied bias V for a substrate-supported and suspended device. The resistance values of both types of structures are on the order of 5kΩ, which is comparable to the sheet resistance values reported for similar layers by Peyyety et al.[21] The bias dependence for suspended constriction is notably different. Above 100 mV bias, the resistance progressively decreases with increasing bias, whereas the resistance of the supported NCG channel remains constant. We attribute this to the lack of thermalization through the substrate, which leads to higher current-induced temperatures in suspended constrictions than in substrate-supported constrictions. We observe a linear dependency for the suspended constriction when plotting the resistance versus electrical power $P=V^2/R$ in Figure 2b. This is understood knowing that the temperature increases to the first order linearly with the dissipated electrical power and that the linear temperature coefficient of the resistivity of NCG at 300 K is negative (α = -0.004 /K), due to thermally activated charge carrier tunneling between nanocrystalline grains, resulting in variable-range hopping within the material,[26,30,31] as shown in Figure 2c.[21] From the electrical heating, we can compare the difference in thermalization between the suspended and supported device. The increase in temperature per power can be calculated from the data in Figure 2b as $dT/dP = 1/R \cdot dR/dP \cdot 1/\alpha$. For the suspended device we obtain 68 $mK\mu W^{-1}$ (dR/dP = -1.4 $\Omega\mu W^{-1}$, R_0 = 5050 Ω @40 μW) and 5 $mK\mu W^{-1}$ (dR/dP = -0.1 $\Omega\mu W^{-1}$, R_0 = 5010 Ω @40 μW) for the substrate-supported. Hence, the thermalization of the suspended device is one order of magnitude lower, showing that for the supported device, the constraint

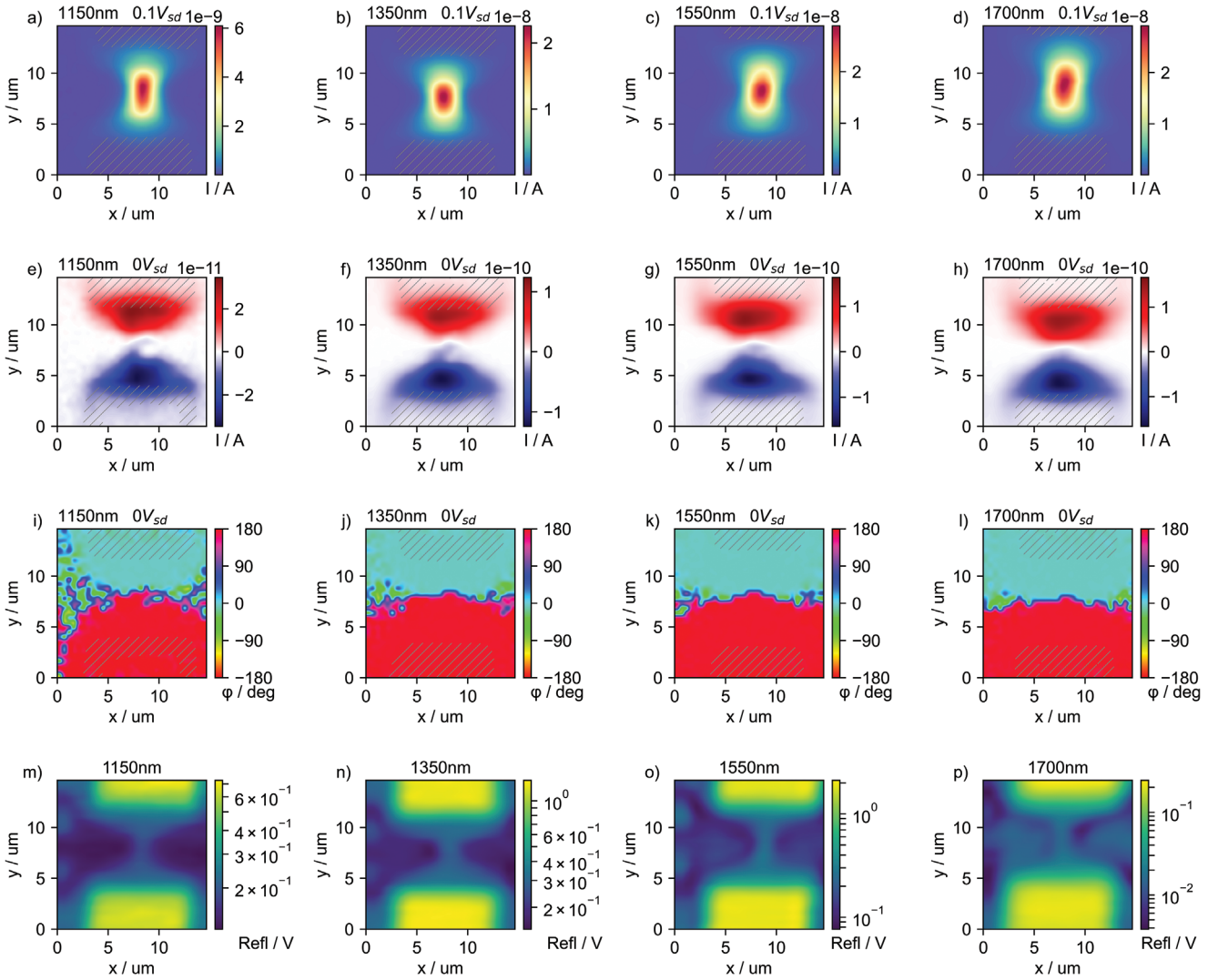

Figure 3. Scanning photocurrent imaging of a substrate-supported constriction device. Data is shown for the wavelengths 1150, 1350, 1550, and 1700nm: a–d) In-phase photocurrent maps measured at 0.1V bias. e–h) Zero-bias in-phase photocurrent maps with corresponding phase maps shown in (i-l). m–p) Reflectance signal, plotted on logarithmic scale. The reflectance signal from the electrodes is overlaid as gray-shaded areas to the maps a-l. Photocurrent maps with logarithmic intensity scale shown in Figure S3 (Supporting Information).

thermalizes mainly through the substrate. The devices were wire-bonded onto a chip carrier for photocurrent measurements and mounted on a customized NIR / SWIR scanning photocurrent imaging and spectroscopy setup. Details are described in the Experimental Section. Briefly, a smooth power spectrum from 1100 to 2100 nm was generated by feeding the light of a broadband supercontinuum laser source into an acousto-optic tunable filter (AOTF). The AOTF was used to adjust the wavelength-specific intensity and to modulate the signal for lock-in detection (see Figure S5, Supporting Information). The smoothened source spectrum was recorded as a reference with a calibrated photodetector to calculate the responsivity. Furthermore, a wavelength-specific correction of chromatic aberration was applied to compensate for the 60 µm axial focus shift across the wavelength range, ensuring diffraction-limited imaging.[21] The fine-tuning of the focus for each wavelength was adjusted by minimizing the laser spot with a 2D SWIR camera. With this focus correction, we performed sequential photocurrent scans of the target area for each wavelength. The photocurrent signal was amplified by a low-noise current preamplifier with adjustable bias (SR570), and the magnitude and phase of the signal were recorded with a lock-in amplifier. The input of the SR570 was connected to the top electrode (w.r.t. **Figures 3** and 4) and the bottom electrode was grounded through a 50 Ω resistor. Applying a positive bias voltage to the top electrode via the SR570 then leads to a technical current that runs through the device from the top electrode to the bottom electrode. This current is recorded by the SR570 as a negative current and is converted into a positive output voltage by activating the invert function. A circuit diagram is shown in **Figure** 5d. The laser signal reflected from the sample surface was detected by a photoreceiver to get simultaneously a reflectance image of the sample surface for correlating the photocurrent signal with the image and the positions of the metal electrodes.

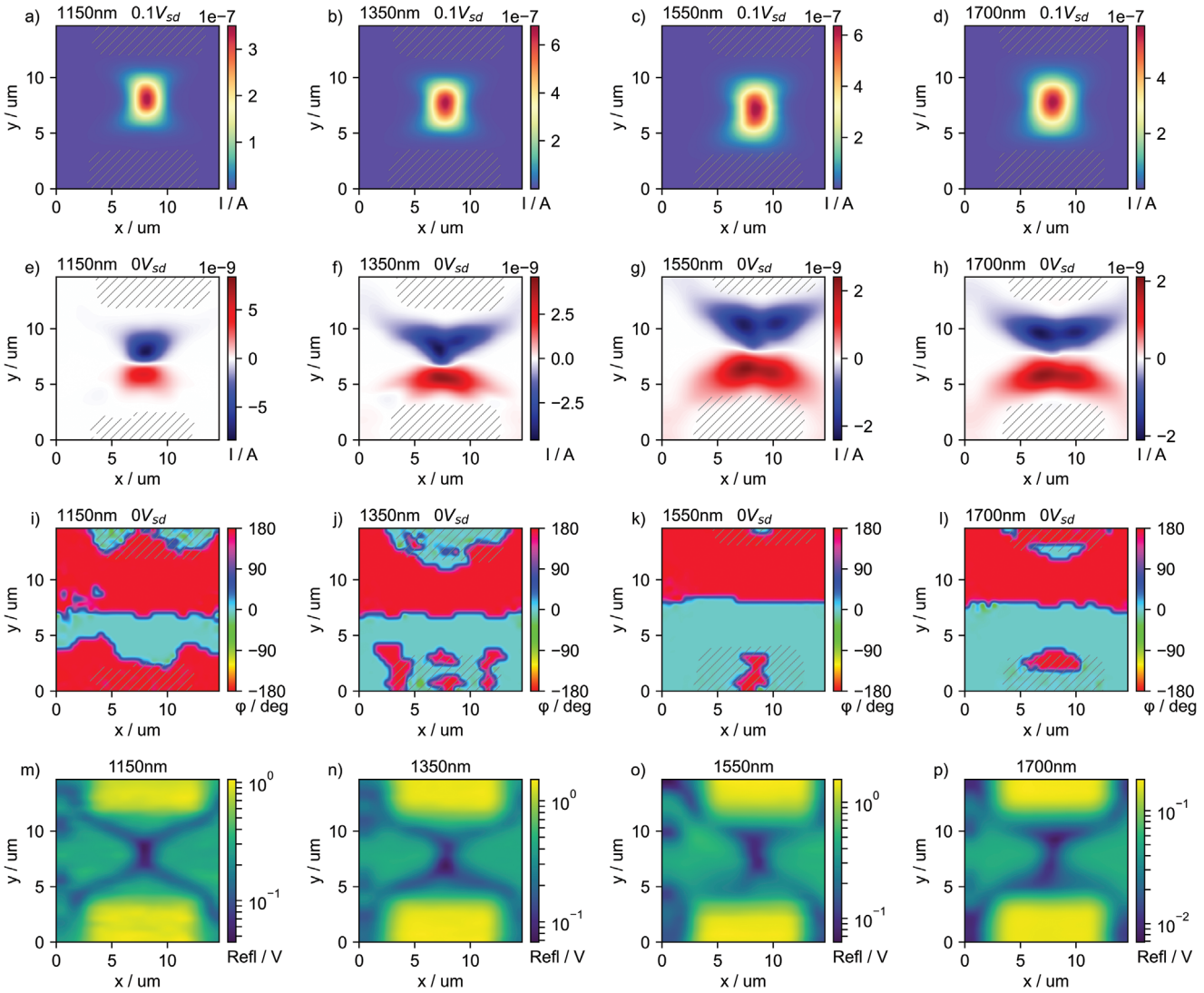

Figure 4. Scanning photocurrent imaging of a suspended constriction device. As in Figure 3, data is shown for the wavelengths 1150, 1350, 1550, and 1700nm: a–d) In-phase photocurrent maps measured at 0.1V bias. e–h) Zero-bias in-phase photocurrent maps with corresponding phase maps shown in (i-l). m–p) Reflectance signal, plotted on logarithmic scale. The reflectance signal from the electrodes is overlaid as gray-shaded areas to the maps a-l. Photocurrent maps with logarithmic intensity scale shown in Figure S4 (Supporting Information).

We first discuss the photocurrent measured on devices with substrate-supported constrictions. Figure 3a–d shows a series of in-phase photocurrent images recorded at 100 mV source-drain bias. For the short-circuit condition (zero bias) we plot the in-phase photocurrent in Figure 3e–h, and the phase between the photocurrent signal and the modulated light signal in Figure 3i–l. All scans were performed over a 15 μm × 15 μm area, with a step size of 500 nm, for wavelengths 1150, 1350, 1550, and 1700 nm. To provide spatial context, electrode positions were determined simultaneously for each scan using reflectance measurements, shown in Figure 3m–p. The signal reflected from the electrodes is overlaid as gray-shaded areas onto the respective photocurrent images. We observed unipolar photocurrents for the biased condition and positive and negative photocurrents for the zero-bias condition, and we identified the photocurrent generation mechanism as bolometric and photo-thermoelectric, respectively. Unlike previous works,[21] the NCG has been shaped in such a way that the signal is generated at the small constriction at the center of the device and not at the NCG/metal contacts. The reason is given by the bolometric photocurrent density,[21]

$$\vec{j}_{bol} = -\alpha \times \rho^{-1} \times \Delta T \times \vec{E} \quad (1)$$

which depends on the linear temperature coefficient α, the resistivity ρ, the photo-induced temperature change ΔT, and the electric field E. The bolometric photocurrent is thus directly proportional to the local electric field and absent in regions devoid of an electric field. By creating a small constriction one can therefore locally enhance the electric field and restrict the bolometric photocurrent signal to the constriction region, which we have verified by simulating the lateral electric field distribution in the patterned NCG with the finite-element method

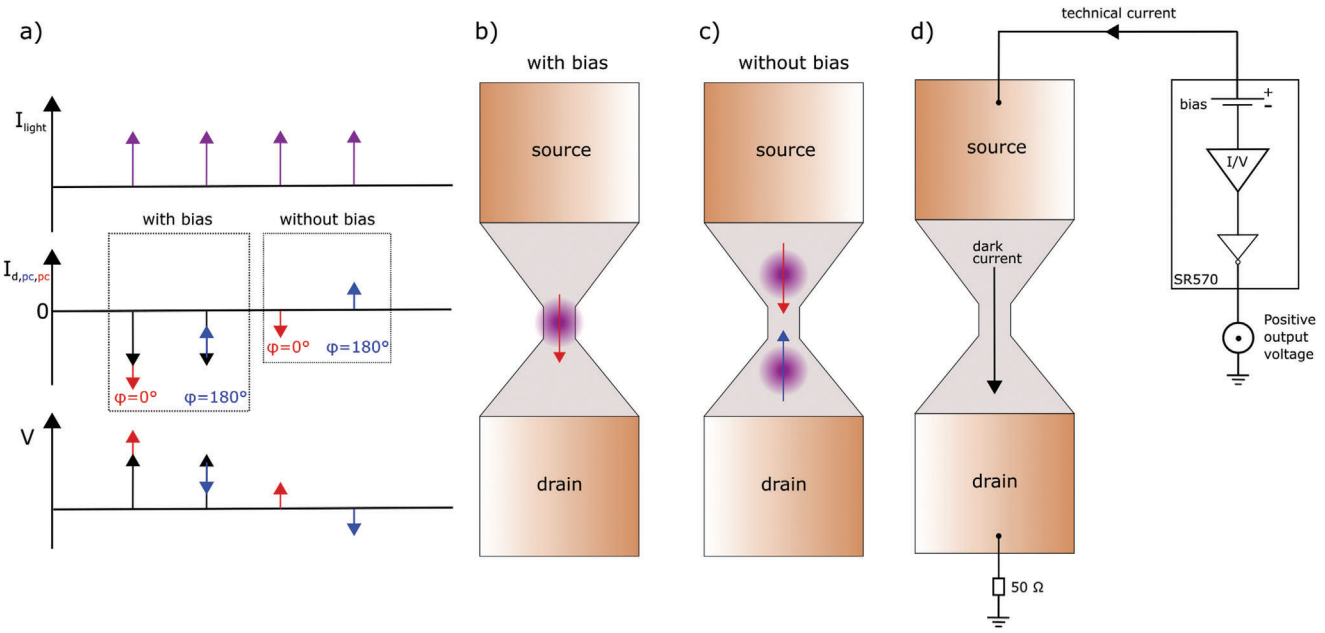

Figure 5. Determine photocurrents with phase-sensitive measurements. a) Correlation between the photocurrent signal I_{PC}, induced by light signal I_{light}, and the output voltage V of the transimpedance preamplifier. The output signal is analyzed with a lock-in amplifier. For the preamplifier configuration shown in d), a positive output signal is generated by a current that follows the technical current direction, corresponding to a photocurrent signal that is in phase with the light signal (ϕ=0°). For a positive bias voltage, a dark current I_{PC} (black arrow) flows from source to drain and has the same direction as the bolometric I_{PC} shown in b), under illumination at the constriction center. c) shows the direction of zero-bias photocurrents for off-center illumination. The current directions for ϕ=0° and ϕ=180° are indicated by red and blue arrows, respectively.

(Figure S1, Supporting Information). The simulation shows that the electric field reaches on the order of 10^4 Vm^{-1} for 100 mV applied bias. The phase of the bolometric photocurrent is close to zero, meaning that the current increases when the light is on, which is consistent with the negative linear temperature coefficient of NCG. Interestingly, the generation of photothermoelectric current (PTE) (measured with zero bias), shown in Figure 3e–h, is also localized around the constriction and not at the NCG/metal contacts, as is the case for NCG devices without constriction (see Figure 4 in Peyyety et al.[21]). The generation of PTE current is even more localized around the constriction for the under-etched device, shown in Figure 4e–h. For the analysis it is important to understand that a local photo-heating induced PTE voltage will give rise to a net PTE current only at an interface between regions with different Seebeck coefficients, where the PTE voltage is then given by,

$$V_{PTE} = (S_2 - S_1) \times (T_{el,1} - T_{el,0}) \quad (2)$$

After photoexcitation, the electron distribution is characterized by an elevated electron temperature $T_{el,1}$, compared to the electron temperature without photoexcitation $T_{el,0}$. Following local photoexcitation and carrier heating, diffusion occurs between the photoexcited "hot" region and the non-photoexcited region, driven by the Seebeck coefficient S. When a homogeneous layer is locally photoexcited, radial charge carrier diffusion takes place, resulting in no net photocurrent because of the isotropic charge current density. However, an anisotropic charge current density is generated when an interface between regions with different Seebeck coefficients, S_1 and S_2, is photoexcited. Note that at NCG/metal contacts, PTE currents are generated due to the different Seebeck coefficients between NCG and metal, leading to photocurrents with opposite polarity when heating each contact separately by local illumination.[21] Here, the PTE photocurrent is generated rather between the metal electrodes and not underneath the NCG/metal contact.[21] The Seebeck coefficient must thus vary within the NCG layer, which could be due to metal-induced doping, as observed in graphene close to graphene/metal contacts.[32]

Now, we discuss the measurements performed on devices with suspended constrictions (Figure 4) and compare them with devices with substrate support (Figure 3). On devices with suspended constrictions (Figure 4a–d), the in-phase bolometric photocurrent is visibly more localized at the constriction and about one order of magnitude more intense than in devices with substrate-supported constriction (Figure 3a–d). This is a direct consequence of the reduced thermalization of the suspended constriction, which leads not only to a marked increase in temperature during current biasing, as discussed in Figure 2b. It also leads to a more pronounced increase in temperature during illumination and hence to a larger bolometric photocurrent, as a consequence of Equation (1). We can quantify the increase of temperature ΔT due to photo-heating from the relative change in resistance $\Delta R / R = (I_d - (I_{PC} + I_d)) / I_d = -I_{PC} / I_d$, with the photocurrent I_{PC} and the dark current I_d (bias voltage drops out). With $\Delta T = -I_{PC} / I_d \times 1/\alpha$ we obtain for the 1550 nm data: ΔT = 7.5 K for the suspended and ΔT = 0.4 K for the supported device. This agrees very well with the thermalization-dependent electrical transport data, taking into account that ≈ 50% of the light power is absorbed by the constriction. Note that the suspended

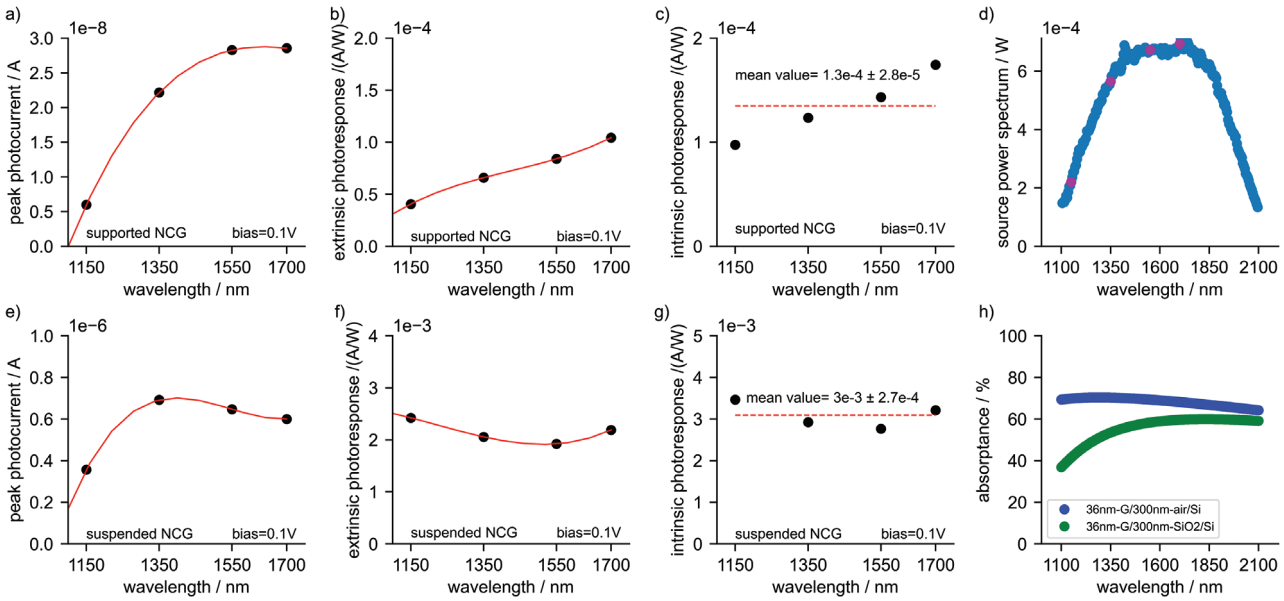

Figure 6. Photocurrent responsivity and spectroscopic analysis. Data from substrate-supported devices (a-c), and suspended constriction devices (e-g). a,e) In-phase photocurrent from the center of Figures 3a-d and 4a-d. b,f) Extrinsic photoresponse from normalization of the peak photocurrent with the fractional power spectrum (see text). d) Power spectrum of the light source (for the intensity adjustment, see supporting information). c,g) Intrinsic photoresponse from the normalization of the extrinsic photoresponse with the graphite absorptance. h) Absorptance of graphite simulated for suspended NCG (35nm-G/300nm-air/Si), and substrate-supported NCG (35nm-G/300nm-SiO_2/Si).

constriction, where the bolometric photocurrent is enhanced, is seen in the reflectance images as a dark area in the center of the Figure 4m–p, while the supported constriction in Figure 3m–p appears as a barely visible, slightly brighter region in the center. This is because the suspended NCG on 300nm-air/Si absorbs more light in the NIR-SWIR wavelength range than the substrate-supported NCG on 300nm-SiO_2/Si, which is a result of optimizing the NCG layer thickness and has been verified by transfer-matrix calculations shown in **Figures 6**h. Furthermore, because the reflectance of Si (0.3@1550nm) is larger than the reflectance from 300nm-SiO_2/Si (0.07@1550nm), the Si regions to the left and right of the constriction in Figure 4m–p (SiO_2 removed by etching) appear brighter than the corresponding 300nm-SiO_2/Si regions in Figure 3m–p. The reduced thermalization at the suspended constriction not only enhances the bolometric photocurrent, but due to Equation (2), it also enhances the PTE current by an order of magnitude as shown in Figure 4e–h. Interestingly, the PTE photocurrent is generated far away from the NCG/metal contacts in the suspended constriction, which excludes metal-induced doping[32] as a possible source for a local variation of the Seebeck coefficient. Furthermore, the phase pattern shown in Figure 4i–l is more complex compared to the substrate-supported data Figure 3i–l. From the top to the bottom electrode of the supported device, the phase changes 0° to 180°, whereas for the suspended device it changes top to bottom from 0° to 180° to 0° to 180°. The data clearly shows that phase shifts are inverted at the suspended constriction, which points to a different origin of PTE for the suspended constriction. Interestingly, when looking at the logarithmic intensity scaling in Figure S4e,f (Supporting Information), one observes that there are sign changes in the phase occurring along the x-direction, which lead to an overall reduction in the PTE current at shorter wavelength. Unfortunately, due to the diffraction limit, it is difficult to resolve the origin, but it is likely related to the wavy edges that give rise to the interference pattern in the optical images (Figure 1a, right). The periodicity of those waves is about 2.4 µm and leads to a locally varying light absorption and hence temperature distribution. Similar ripples at edges of nanocrystalline graphite have been observed previously and are due to compressive strain formed during the synthesis of the material.[28] Recently, geometrically-induced spatial variation of the Seebeck coefficient was reported for a graphene bowtie constriction,[33] and similar effects have also been observed in metal-nanowire constrictions,[34] and in silicon nanoconstrictions.[35] The spatial variations of the Seebeck coefficient in such nanoscale constrictions are attributed to local variation in the mean-free path due to scattering at surfaces, edges, or grain boundaries.[34] A similar mechanism could lead to the enhanced photo-thermoelectric current generation at suspended NCG constrictions. However, one should also keep in mind that the thermalization must spatially vary for the under-etched constriction and that a strong temperature gradient is expected when locally heating the upper or lower part of the constriction. This could then lead to a PTE signal without the Seebeck coefficient being spatially varying. A comment on the meaning of the phase and its relation to the current direction. From the dark measurement and the bolometric photocurrent measurement, we know that photo-induced currents flowing in the same direction as the dark current produce a zero phase signal, whereas photocurrents flowing in the opposite direction yield a phase of 180°. Hence from the maps of the phase, we can directly deduce the direction of the photocurrent: top to bottom for 0° and bottom to top for 180°, as explained in Figure 5a–c.

Finally, we quantify the responsivity of the devices from the bolometric photocurrent at the center of the Figures 3 and 4. The

Table 1. Comparison of 2D/thin film photodetectors.

Material	wavelength [nm]	incident power [mW]	bias [V]	responsivity [A/W]	detectivity [D*]	ref
Graphene	1550	10	0.4(Vg=-15V)	6×10^{-3}	1.8×10^{8}	[38]
MoS_2	445-2717	8	10	32.5×10^{-2}	9.6×10^{8}	[39]
Black Phosphorous	1550	1.91	0.4(Vg=-8V)	1.4×10^{-3}	6.7×10^{10}	[40]
Bi_2Te_3	1064-1550	0.67-2.8	0.1	3.6×10^{-3}	–	[41]
suspended NCG	1100-1700	0.1-0.7	0.1	3×10^{-3}	1.2×10^{9}	this work

maximum photocurrent values for the four wavelengths are plotted in Figure 6a,e for the supported and suspended NCG devices, respectively. The extrinsic photoresponse Figure 6b,f was calculated by normalizing the maximum photocurrent for each wavelength with the corresponding source power values Figure 6d, and by taking into account that 39–67 % of the incoming light falls onto the center 2 µm x 2 µm area. The fractional values were calculated from the Gaussian beam diameter, and the beam diameter was measured for each wavelength by scanning the beam across a reflective edge (see Figure S2, Supporting Information). The intrinsic photoresponse Figure 6c,g was then calculated by normalizing the extrinsic photocurrent with the percentage of light that was absorbed by the NCG layer. The absorptance, shown in Figures 6h, was calculated by the transfer matrix method for the NCG layer thickness of 36 nm. The thickness was optimized for flat absorptance in the NIR-SWIR wavelength range for the suspended NCG (36nm-NCG/300nm-air/Si) and yields (70 ± 6) %. As a result, the extrinsic and the intrinsic responsivity are both flat for the suspended device, resembling an ideal bolometric detector, where the photocurrent is proportional to the absorbed power and hence wavelength-independent. Moreover, the bolometric and PTE currents are both increasing linearly with laser power for excitation above 10% of the maximum laser output, which can be seen in Figure S6 (Supporting Information). The mean intrinsic photoresponse for the device with suspended constriction is $(3 \pm 0.3) \times 10^{-3}$ AW^{-1}, which is over an order of magnitude higher than for the device with supported constriction. This difference is attributed to reduced thermalization by the substrate, as discussed. The comparison to previous work without constriction is not trivial. Here, in this work, the central device area is comparable to the beam diameter, whereas often the device area is larger than the beam diameter. If the step size for scanning a large area is comparable to the beam diameter, then the integrated photocurrent can be used to determine the responsivity.[21] Note also that the responsivity scales with the voltage bias, and that a large responsivity at low voltage bias is preferred for a low-power photodetector. Unfortunately, the full details are not always given and the responsivities are sometimes overestimated and/or difficult to compare.[36] We nevertheless compiled a short list of operation and performance parameters of 2D/thin film NIR-SWIR photodetectors in **Table 1**. Last, we have determined the specific detectivity D* which is an important figure of merit for sensing low light levels. For a shot-noise limited device as in this case, D* is calculated as[37]

$$D^* = R/\sqrt{2 \times q \times I_d} \tag{3}$$

with the responsivity R, the elementary charge q, the detector area A, and the dark current I_d. With $R = 3 \times 10^{-3}$ AW^{-1}, and $I_d = 20$ µA, we obtain 1.2×10^{9} Jones at 0.1 V bias, which is more than one order of magnitude larger compared to the substrate-supported devices with constriction (4.0×10^{7} Jones), and three orders of magnitudes larger compared to supported devices without constriction (2.1×10^{6} Jones).[21] This shows that tailoring the geometry and thermal decoupling has a huge impact on device performance. In the future, the device performance could be further improved by incorporating a reflective layer (i.e., gold) at the bottom of the air gap, which would result in nearly complete light absorption while maintaining spectral flatness.

3. Conclusion

The benefit of using nanocrystalline graphene as a photoabsorber material is that its thickness can be adjusted on a waferscale to achieve a flat absorptance in the NIR-SWIR wavelength range. In addition, the material is compatible with CMOS processing and can be laterally shaped and made free-standing via dry and wet etching processes. This allowed the fabrication of freestanding bowtie constrictions with thickness-adjusted absorptance, and enabled orders of magnitude enhanced responsivity and detectivity compared to substrate-supported devices, as a result of an order of magnitude reduced thermalization of the suspended constriction. Moreover, by focusing the electric field on a narrow region, the bolometric photocurrent is generated at the constriction remote from the electrodes. We also observe a strongly enhanced photothermoelectric current generation at the constriction with inverted phase angles, which might be due to either an asymmetric temperature gradient or a local variation of the Seebeck coefficient. In the future, further enhancements are feasible by reducing the resistivity of the material through grain size and grain boundary engineering, and by further increasing light absorption close to unity through the addition of a reflective coating at the bottom of the air gap.

4. Experimental Section

NCG Synthesis, Characterization and Device Fabrication: Thermally grown 300 nm SiO_2 on p-Si (boron doping, $\rho < 0.005$ Ωcm, Active Business Company) wafers were cut into 10 mm × 10 mm size, sonicated in acetone, rinsed with isopropanol, and exposed to a mild oxygen plasma. A pre-baking step at 110 °C on a hot plate for 120 s removed the physisorbed water. NCG films were grown on the soft-baked SiO_2/Si substrates using the S1805 photoresist (MICROPOSIT) as a carbon source. The photoresist was diluted 1:1 with propylene glycol mono-methyl ether acetate (PGMEA), and 35 µL of the prepared resist solution was spin-coated at 4000

rpm for 30 s to target final NCG thicknesses of 35 nm. The spin-coated substrates were baked at 110 °C for 60 s on a hot plate to allow outgassing of the solvent. After the post-baking step, the substrates were loaded into the vacuum furnace for graphitization of the photoresist film at 1000 °C at 10^{-6} mbar pressure. The thickness of the synthesized NCG film was measured using the atomic force microscope (Bruker Dimension Icon) in the tapping mode. The NCG films were characterized using Raman spectroscopy (Renishaw inVia Microscope) at 532 nm laser excitation, 3 mW power, 10 s integration time, and 100× (NA = 0.85) magnification. The device fabrication on the substrates with the NCG film was realized by depositing metal electrodes and alignment markers, and subsequent etching of the NCG. Gold electrodes and markers were defined by spin-coating poly(methyl methacrylate) (PMMA 950 k, 4.5% in anisol) at 6000 rpm for 60 s on NCG/SiO_2/Si and pre-baked on a hot plate for 3 min at 150°C to give a 210 nm thick resist layer. With electron-beam lithography (LEO 1530 with Raith ELPHY Plus pattern generator) the resist was patterned, and the e-beam exposed areas were developed in a solution of methyl isobutyl ketone (MIBK) / isopropanol (IPA), ratio 1:3, at 0°C for 30 s, rinsed with IPA, dried in a nitrogen stream and post-baked on a hot plate for 1 min at 90°C. 5 nm Cr and 50 nm Au were deposited by electron-beam physical vapor deposition, and the lift-off was done in acetone. To etch the NCG into the desired shape, poly(methyl methacrylate) (PMMA 950 k, 8% in anisol) was spin-coated at 6000 rpm to form a 700 nm thick layer. After the EBL writing step, the pattern was developed in a solution of MIBK/IPA (ratio 1:3) for 30 s and subsequently baked on a hotplate for 60 s at 90°C. The unprotected areas of NCG were etched by O_2 plasma in a reactive-ion etching (Oxford Plasmalab 80 Plus and Pro 80 ICP) at 15 sccm O_2, 60 mTorr, 30 W RF and 183 V DC bias, 4 min and 15 s. The remaining PMMA after the etching step was removed by acetone. The NCG channels were suspended by chemical wet etching of SiO_2. Once again the PMMA 4.5 spin-coated on the substrate and electron beam patterning was done to expose the areas to etch SiO_2. After developing the pattern, commercial Buffered oxide etch (BOE 6:1) (J.T.Baker company) was used to etch SiO_2 under the NCG channel 300 nm vertically and 2 µm laterally. This wet etching process was isotropic. The sample was placed in the Teflon bowl shape container and a drop of BOE 6:1 was placed on the sample for 10min. After the etching process, the sample was cleaned with double distilled water.

Photocurrent Measurements and Electrical Characterization: The photocurrent maps were recorded in the NIR/SWIR spectral range from 1100 to 2100 nm using a SC white-light source (SuperK Extreme EXW-12, NKT Photonics). An AOTF (SuperK Select-nIR2 AOTF attached to SuperK connector with FD6-PM fiber) converts the SC white-light source into a tunable laser source. The excitation laser line from the AOTF was then coupled to a reflective collimator (Thorlabs RC02FC-P01), and 90% of the collimated light is guided through the 90:10 beam splitter (Thorlabs BS030) into the customized Zeiss Axiotech VARIO microscope with an NIR objective. The laser source intensity was continuously monitored during the photocurrent scan using a NIR photodiode sensor (PD300R-IR, Ophir) attached at the 10% exit port. The photocurrent maps were recorded in 200 nm wavelength steps. The laser spot limited by diffraction was focused on the sample using the infinity-corrected 100× NIR (Mitutoyo M PLAN APO, 0.50 NA) long working distance objective, and the laser spot was positioned across the scan area (15 µm × 15 µm) with a stepper motor-controlled X–Y translation stage (8MTF-102LS05, Standa) in 0.5 µm steps. A motorized z-stage (KVS30, Thorlabs) was used to control the vertical position with 0.1 µm precision. The laser spot reflected from the sample surface was imaged using a Peltier-cooled InGaAs camera (WiDy Sens 640V-ST, New Imaging Technologies). The fine adjustment of the focus was precisely controlled using a piezo objective scanner (PIFOC P-712.CDQ, Physik Instrumente). The chromatic aberration-induced shift of the axial focus of the NIR objectives was compensated for each wavelength before obtaining a photocurrent map. A wavelength–specific intensity adjustment to the AOTF was implemented to obtain a smooth, intensity-calibrated source spectrum (Figure S5, Supporting Information). The photocurrent of the NCG film was measured using the lock-in technique at room temperature. The incident light was modulated at 1.111 kHz via the AOTF SuperK COMMAND interface box. The frequency was selected in a low-noise region remote from multiple power line signals analyzed using a spectrum analyzer (Signal Hound USB-SA44B) at the lock-in monitor output. The modulated photocurrent was converted into a voltage signal using a low-noise current preamplifier (SR570, Stanford Research Systems) and fed into the lock-in amplifier (SR830 Lock-in Amplifier, Stanford Research Systems) referenced to the modulation frequency. The photocurrent amplitude and phase were subsequently recovered from the lock-in amplifier. For biased photocurrent measurements, a bias was applied via the SR570. A circuit diagram is shown Figure 5d. In sync with the photocurrent mapping, the back-reflected light from the sample was simultaneously recorded to map out the device area using an InGaAs photoreceiver (OE-200-IN2, Femto) connected to the source meter (Keithley 6430). The photocurrent and reflectance mapping were automated and controlled using a Python code. Electrical characterization was conducted using an Agilent 4155C semiconductor parameter analyzer system and a probe station with TRIAX probes with a low current detection limit of 30 fA.

Simulations: Transfer matrix method (TMM) simulations were conducted for s-polarized light at normal incidence using a Python code available at github.com/krupke-group based on the TMM code of Steve Byrnes (arXiv:1603.02720; github.com/sbyrnes321/tmm). The complex refractive index of NCG was approximated by the optical constants of graphite, calculated from an analytical expression based on the dynamical conductivity of graphite.[18] The optical constants for Si and SiO_2 were taken from the refractiveindex.info database (SiO_2: Lemarchand 2013, Si: Aspnes and Studna 1983), extended with NIR data for Si from the filmetrics.de database. FEM simulations of the electric field distribution were performed using the commercial FlexPDE 6.5 software package. The 2D simulation space was confined by two Dirichlet boundaries, defining the potential difference from the applied bias voltage, and by Neumann boundaries for the noncontacted sides. Inside the boundaries, the material was defined by its resistivity.

Statistical Analysis: The Experimental Section contains comprehensive information about device dimensions, materials, and fabrication processes. The presented photocurrent maps were highly reproducible since repeated measurements on the same device area were not distinguishable. Charge transport data varied from device to device by less than 10 % in terms of the device resistance. The data were plotted using standard Python libraries commonly used in the field like numpy, pandas, and matplotlib.

Supporting Information

Supporting Information is available from the Wiley Online Library or from the author.

Acknowledgements

D.P., S.K., S.D., and R.K. acknowledged support by the Helmholtz Research Programs Natural, Artificial and Cognitive Information Processing (NACIP) and Materials Systems Engineering (MSE), and by the Karlsruhe Nano Micro Facility (KNMF).

Open access funding enabled and organized by Projekt DEAL.

Conflict of Interest

The authors declare no conflict of interest.

Author Contributions

The experiments were conceived and designed by R.K. and D.P. Devices were fabricated by D.P. and S.D. and characterized by D.P. The NCG synthesis was performed by S.K. The manuscript was written by R.K. and D.P. with input from all co-authors.

Data Availability Statement

The data that support the findings of this study are available from the corresponding author upon reasonable request.

Keywords

bolometric photodetection, nanocrystalline graphene, NIR, photocurrent spectroscopy, SWIR

Received: August 31, 2023
Revised: October 20, 2023
Published online: November 20, 2023

[1] R. Ramaswami, *IEEE Commun. Mag.* **2002**, *40*, 138.
[2] Y. Chen, S. Wang, F. Zhang, *Nat. Rev. Bioeng.* **2023**, *1*, 60.
[3] J.-H. Qu, D. Liu, J.-H. Cheng, D.-W. Sun, J. Ma, H. Pu, X.-A. Zeng, *CRC Crit. Rev. Food. Sci. Nutr.* **2015**, *55*, 1939.
[4] Z. Zhao, Z. Zhang, J. Jing, R. Gao, Z. Liao, W. Zhang, G. Liu, Y. Wang, K. Wang, C. Xue, *APL Mater.* **2023**, *11*, 21107.
[5] A. A. Munawar, Y. Yunus, D. Devianti, P. Satriyo, *IOP Conf. Ser.: Earth Environ. Sci* **2021**, *644*, 12036.
[6] I. Gatley, D. L. Depoy, A. M. Fowler, *Science* **1988**, *242*, 1264.
[7] C. Downs, T. E. Vandervelde, *Sensors* **2013**, *13*, 5054.
[8] C. Liu, J. Guo, L. Yu, J. Li, M. Zhang, H. Li, Y. Shi, D. Dai, *Light Sci. Appl.* **2021**, *10*, 123.
[9] G. Konstantatos, *Nat. Commun.* **2018**, *9*, 5266.
[10] K. Zhang, Z. Hu, L. Zhang, Y. Chen, D. Wang, M. Jiang, G. D'Olimpio, L. Han, C. Yao, Z. Chen, H. Xing, C. N. Kuo, C. S. Lue, I. Vobornik, S. W. Wang, A. Politano, W. Hu, L. Wang, X. Chen, W. Lu, *Small* **2023**, *19*, 2205329.
[11] Z. Hu, L. Zhang, A. Chakraborty, G. D'Olimpio, J. Fujii, A. Ge, Y. Zhou, C. Liu, A. Agarwal, I. Vobornik, D. Farias, C. N. Kuo, C. S. Lue, A. Politano, S. W. Wang, W. Hu, X. Chen, W. Lu, L. Wang, *Adv. Mater.* **2023**, *35*, 2209557.
[12] L. Wang, L. Han, W. Guo, L. Zhang, C. Yao, Z. Chen, Y. Chen, C. Guo, K. Zhang, C. N. Kuo, C. S. Lue, A. Politano, H. Xing, M. Jiang, X. Yu, X. Chen, W. Lu, *Light: Sci. Appl.* **2022**, *11*, 1.
[13] F. Bonaccorso, Z. Sun, T. Hasan, A. C. Ferrari, *Nat. Photonics* **2010**, *4*, 611.
[14] S. Thongrattanasiri, F. H. L. Koppens, F. J. de Abajo, *Phys. Rev. Lett.* **2012**, *108*, 47401.
[15] M. Long, P. Wang, H. Fang, W. Hu, *Adv. Funct. Mater.* **2019**, *29*, 1803807.
[16] M.-K. Zhang, W.-D. Liu, Y.-P. Gong, Q. Liu, Z.-G. Chen, *Adv. Opt. Mater.* **2022**, *10*, 2201889.
[17] F. H. L. Koppens, T. Mueller, P. Avouris, A. C. Ferrari, M. S. Vitiello, M. Polini, *Nat. Nanotechnol.* **2014**, *9*, 780.
[18] K. Sasaki, K. Hitachi, *Commun. Phys.* **2020**, *3*, 1.
[19] A. Riaz, F. Pyatkov, A. Alam, S. Dehm, A. Felten, V. S. K. Chakravadhanula, B. S. Flavel, C. Kübel, U. Lemmer, R. Krupke, *Nanotechnology* **2015**, *26*, 325202.
[20] Z. Zhang, B. Ge, Y. Guo, D. Tang, X. Wang, F. Wang, *Chem. Commun.* **2013**, *49*, 2789.
[21] N. A. Peyyety, S. Kumar, M. K. Li, S. Dehm, R. Krupke, *ACS Appl. Mater. Interfaces* **2022**, *14*, 9525.
[22] M. Freitag, T. Low, P. Avouris, *Nano Lett.* **2013**, *13*, 1644.
[23] A. C. Ferrari, J. Robertson, *Phys. Rev. B Condens. Matter Mater. Phys.* **2001**, *64*, 1.
[24] C. N. S. Kumar, V. S. K. Chakravadhanula, A. Riaz, S. Dehm, D. Wang, X. Mu, B. Flavel, R. Krupke, C. Kübel, *Nanoscale* **2017**, *9*, 12835.
[25] C. N. S. Kumar, M. Konrad, V. S. K. Chakravadhanula, S. Dehm, D. Wang, W. Wenzel, R. Krupke, C. Kübel, *Nanoscale Adv.* **2019**, *1*, 2485.
[26] S. Kumar, Ph.D. Thesis, Technische Universität, Darmstadt **2022**.
[27] X. L. Li, X. F. Qiao, W. P. Han, Y. Lu, Q. H. Tan, X. L. Liu, P. H. Tan, *Nanoscale* **2015**, *7*, 8135.
[28] R. Yekani, E. Rusak, A. Riaz, A. Felten, B. Breitung, S. Dehm, D. Perera, J. Rohrer, C. Rockstuhl, R. Krupke, *Nanoscale* **2018**, *10*, 12156.
[29] O. M. G. Ward, E. McCann, *J. Phys. D Appl. Phys.* **2021**, *54*, 475303.
[30] J. Zhao, C. He, R. Yang, Z. Shi, M. Cheng, W. Yang, G. Xie, D. Wang, D. Shi, G. Zhang, *Appl. Phys. Lett.* **2012**, *101*, 063112.
[31] S. Nakamura, D. Miyafuji, T. Fujii, T. Matsui, H. Fukuyama, *Cryogenics* **2017**, *86*, 118.
[32] K. J. Tielrooij, M. Massicotte, L. Piatkowski, A. Woessner, Q. Ma, P. Jarillo-Herrero, N. F. van Hulst, F. H. L. Koppens, *J. Phys. Condens. Matter* **2015**, *27*, 164207.
[33] A. Harzheim, J. Spiece, C. Evangeli, E. McCann, V. Falko, Y. Sheng, J. H. Warner, G. A. D. Briggs, J. A. Mol, P. Gehring, O. V. Kolosov, *Nano Lett.* **2018**, *18*, 7719.
[34] P. Zolotavin, C. Evans, D. Natelson, *J. Phys. Chem. Lett.* **2017**, *8*, 1739.
[35] H. Xue, R. Qian, W. Lu, X. Gong, L. Qin, Z. Zhong, Z. An, L. Chen, W. Lu, *Nat. Commun.* **2023**, *14*, 3731.
[36] F. Wang, T. Zhang, R. Xie, Z. Wang, W. Hu, *Nat. Commun.* **2023**, *14*, 2224.
[37] X. Gong, M. Tong, Y. Xia, W. Cai, J. S. Moon, Y. Cao, G. Yu, C.-L. Shieh, B. Nilsson, A. J. Heeger, *Science* **2009**, *325*, 1665.
[38] T. Mueller, F. Xia, P. Avouris, *Nat. Photonics* **2010**, *4*, 297.
[39] Y. Xie, B. Zhang, S. Wang, D. Wang, A. Wang, Z. Wang, H. Yu, H. Zhang, Y. Chen, M. Zhao, B. Huang, L. Mei, J. Wang, *Adv. Mater.* **2017**, *29*, 1605972.
[40] N. Youngblood, C. Chen, S. J. Koester, M. Li, *Nat. Photonics* **2015**, *9*, 247.
[41] J. Liu, Y. Li, Y. Song, Y. Ma, Q. Chen, Z. Zhu, P. Lu, S. Wang, *Appl. Phys. Lett.* **2017**, *110*, 141109.